

Discrete Image Model and Segmentation for Microstructure Features Identification in Ductile Irons

A. De Santis¹, O. Di Bartolomeo², D. Iacoviello¹, F. Iacoviello²

¹Dept. Informatica e Sistemistica, University "La Sapienza" of Rome, Via Eudossiana 18 00 184 Roma, Italy

²Dept. Meccanica, Strutture, Ambiente e Territorio-Universita di Cassino, via G.d. Biasio 43, 03043 Cassino, Italy

Ductile irons offer a wide range of mechanical properties at a lower cost than the older malleable iron. These properties mainly depend on the shape characteristics of the metal matrix microstructure and on the graphite elements morphology; these geometrical features are currently evaluated by the experts visual inspection. This work provides an automatic procedure for a reliable estimation of standard parameters of the material microstructure morphology based on a novel image segmentation technique. The procedure has been validated versus standard segmentation techniques, and successfully tested on specimens of different kinds of ductile irons of a typical production.

Keywords: image segmentation, level sets, discrete analysis, material science

1. INTRODUCTION

Image data are largely used almost in any scientific field. Frameworks such as medicine and earth environment monitoring have historically based their investigations on image analysis [1-4]. The industry compartment has increasingly become interested in the application of image processing, as high-level tasks can be accomplished by automation systems using the complex information that can be extracted from image data at a very low cost [5-6]. In particular, quality control fully exploits the chances offered by such a technology for real time detection of the production defects [7-8]. Material science has only recently become aware of the advantages of image analysis: pictures of metallographic planes are processed to extract the information relevant to the characterization of the material mechanical properties [9-11]. This information is currently evaluated by experts visual inspection of specimens obtained by light optical microscope (LOM).

Any application requires the definition of features that compose the information to be extracted from data (intensity, color, texture, motion, topology, geometry,...). The role of image processing therefore consists in separating the elements on a picture according to the "value" assumed by the features of interest; as a consequence a simplified version of the original picture is obtained where all the elements are separated from the context and labeled, so that they can be individually analyzed. This step is called *image segmentation*, see [12] for a reference work on the variational approach. A further step is usually required to link the raw information obtained by the segmentation to the objects properties, relevant to the given application. This is particular evident in the case of the materials considered in this work where the mechanical properties depend on the morphology of their microstructure. The interest in ductile irons relies in their versatility: within the same production process, by

adjusting some parameters, materials with properties varying in a wide range of values can be obtained at a very low cost. The ductile iron basic elements are the metallic matrix and the graphite nodules. The former is responsible for the tensile strength and wear resistance, whereas the latter perform mainly as crack arresters. The matrix properties depend on the *volume fraction* of its phases of different chemical composition; the nodules performance depends on their *shape*. Phases' volume fractions and nodule's morphological parameters can be reliably estimated by image analysis applied to the pictures of the metallographic planes of the material specimens. For quality control routine some quantitative approaches have been proposed in literature, based on the definitions of a shape factor defined as the ratio of the nodule section area over the circumscribed circle area, [9,10]; the role of research activity should aim at the development of a standard methodology to support these quantitative methods.

Images obtained by means of LOM, despite a good visual appearance, are represented by a quite irregular signal due to various kind of degradations stemming from the very acquisition process: additive noise, albedos due to dust and specimen oxidation, artefacts coming from scratches occurring during the specimen preparation. In these conditions methods based on signal thresholding may fail in providing reliable results; global thresholds may also provide results of different quality on different zones of the same specimen; moreover thresholds may change from specimen to specimen. A high performance image analysis procedure to robustly evaluate the nodules shape characteristics and the matrix phases fractions can be obtained within the framework of image segmentation: the original image is partitioned into disjoint domains where the signal has homogeneous characteristics, and, passing from one domain to another, these characteristics vary significantly

[12, 13]. Within each domain a best minimum square fit to the data is also provided so that a *cartoon* image is obtained; this is the closest approximant of the original picture in the class of piecewise constant functions. The segmented image preserves all the graphic information relevant to the analysis to be performed, but with a lower number of different gray levels: for the considered application two levels proved to be sufficient, as compared to 256 levels (8-bit) of the original LOM data. The segmentation problem can be solved by various techniques (see [14]), with different pros and cons. In this paper a region based method was preferred since it can deal with the complex topology of the material specimens and is numerically efficient, [15]: as a consequence the ductile iron metallographies can be reliably segmented and evaluated also in real time. As opposite to standard procedures that are based on a continuum model of the image, the novelty of the proposed method consists in defining the segmentation problem and the related algorithm directly in the discrete domain. Despite the formulation in the continuum allows for a sophisticated analysis, giving ultimately a deep insight into the segmentation problem, the optimal segmentation is obtained as a solution of an evolution equation (the Euler-Lagrange equation related to the variational problem); this solution can only be computed numerically by discretization. Therefore only a numerical approximation of the optimal solution is obtained; this approximation is defined on the lattice where the data are available, so that most of the analytical properties of the continuum image model loose their meaning. To get around these problems, a discrete set up was developed, [15]. The choice of the cost functional and the characterization of the segmentation elements on the discrete domain allows us to obtain the Euler-Lagrange equation directly as a non linear difference equation that, in this case, turns out to be necessary and sufficient for the global minimum in the class of piecewise constant functions, with no restrictions on the nature of the multiple points, so to meet the complex topology of the real world images. This equation is an explicit numerical scheme for the level set function computation, that is the level set samples at step $n + 1$ are explicitly defined as a function of just the same quantities at step n , whereas numerical approximation of continuum partial differential equation usually requires implicit schemes.

Experiments on cast iron specimens showed the inadequacy of simple thresholding procedure, while the performance of the proposed method was satisfactory both in terms of numerical efficiency and segmentation accuracy. The method was also validated by a comparison with a well established region based segmentation procedure, obtaining the same level of performances in the half time. Therefore the shape parameters of the nodules and the volume fractions of the metallic matrix have been reliably estimated on a batch of a typical cast iron production.

The paper is organized as follows. In section 2 a description of the properties of the ductile irons is presented.

In section 3 the proposed image segmentation procedure is outlined. In section 4 real data experiments are provided. Concluding remarks along with some possible further developments are presented in section 5.

2. DUCTILE IRONS DESCRIPTION

Ductile cast irons are characterized by a wide range of mechanical properties, mainly depending on microstructural factors, as graphite particles, phases and defects. Ductile iron advantages that have led to its success are numerous, and they can be summarized easily: versatility and higher performances at lower cost. This versatility is especially evident in the area of mechanical properties where ductile iron offers the designer the option of choosing high ductility (up to 18% elongation), or high strength, with tensile strengths exceeding 825 MPa (mega Pascal). Austempered ductile iron offers even better mechanical properties: higher wear resistance, providing tensile strengths exceeding 1600 MPa. Ferritic-pearlitic ductile irons are widely used because they are able to summarize both a high castability and good mechanical properties (the best combination is obtained with similar ferrite and pearlite volume fraction).

Focusing on graphite elements shape, a very high *nodularity* is strongly recommended. The peculiar morphology of graphite elements in ductile irons is responsible of their good ductility and toughness. Characterized by a rough spherical shape, graphite particles contained in ductile irons are also known as “nodules”. They act as “crack arresters”, with a consequent increase of toughness, ductility and crack propagation resistance [16]. A lack of graphite elements roundness immediately implies a degradation of the mechanical properties. Considering the results of in-situ tensile tests performed on a fully pearlitic ductile iron (Fig. 1, arrows indicate loading direction), it is evident that an irreversible damage (crack) localises in graphite elements in the linear elastic stage, where deformations are usually considered as completely reversible. Crack starts and propagates where the graphite element presents a lack of roundness, and, as a consequence, stress intensification is obtained. Corresponding to higher deformation, where the irreversible strain component is macroscopically evident, damage increases with decohesion of nodules pole cap and a consequent pearlite-graphite debonding. Focusing on the metal matrix microstructure, it could range from fully ferritic, to fully pearlitic, from martensitic to bainitic depending on the chemical composition and on the heat treatment. Microstructure strongly affects mechanical properties and damaging micromechanisms, as it can be observed by comparing the damaging mechanisms shown in Fig.1 (fully pearlitic ductile iron) with the results obtained with a ferritic-pearlitic ductile iron (50% ferrite–50% pearlite), Fig. 2. In this case, the linear stage is not characterized by cracks presence, and damage evolution is mainly connected to decohesion of nodules pole cap and

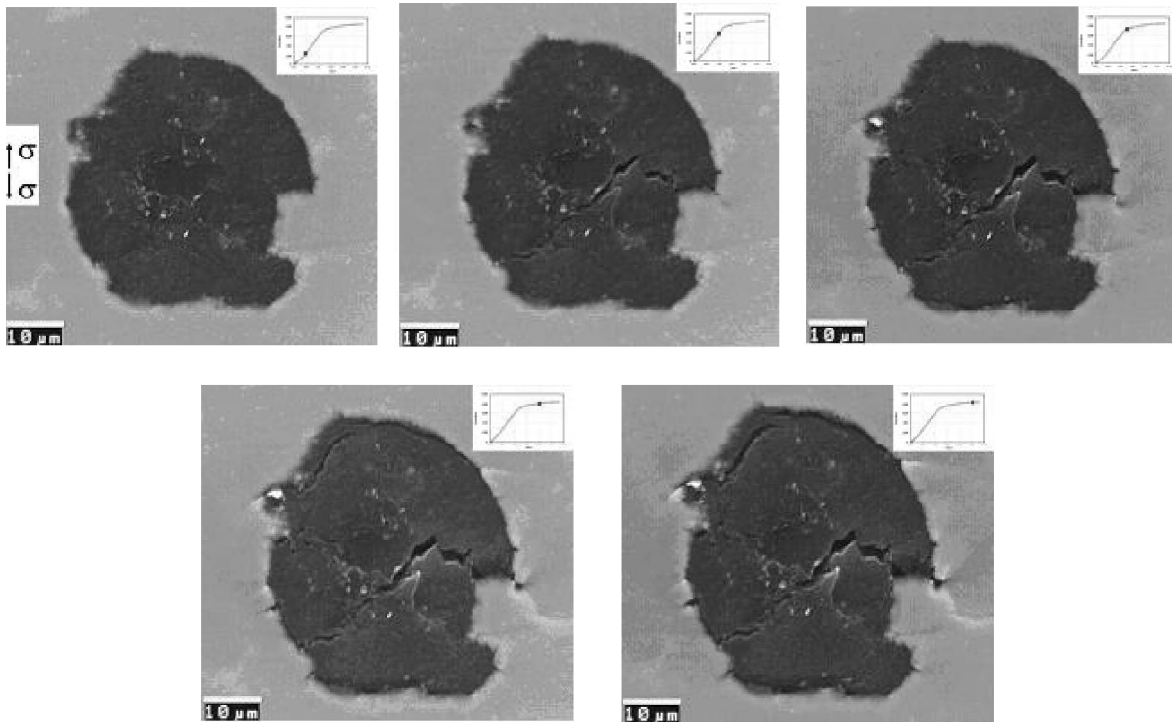


Figure 1: SEM (Scanning Electron Microscope) in-situ surface analysis during a tensile test (strain-stress diagram; fully pearlitic ductile iron): graphite element damage evolution

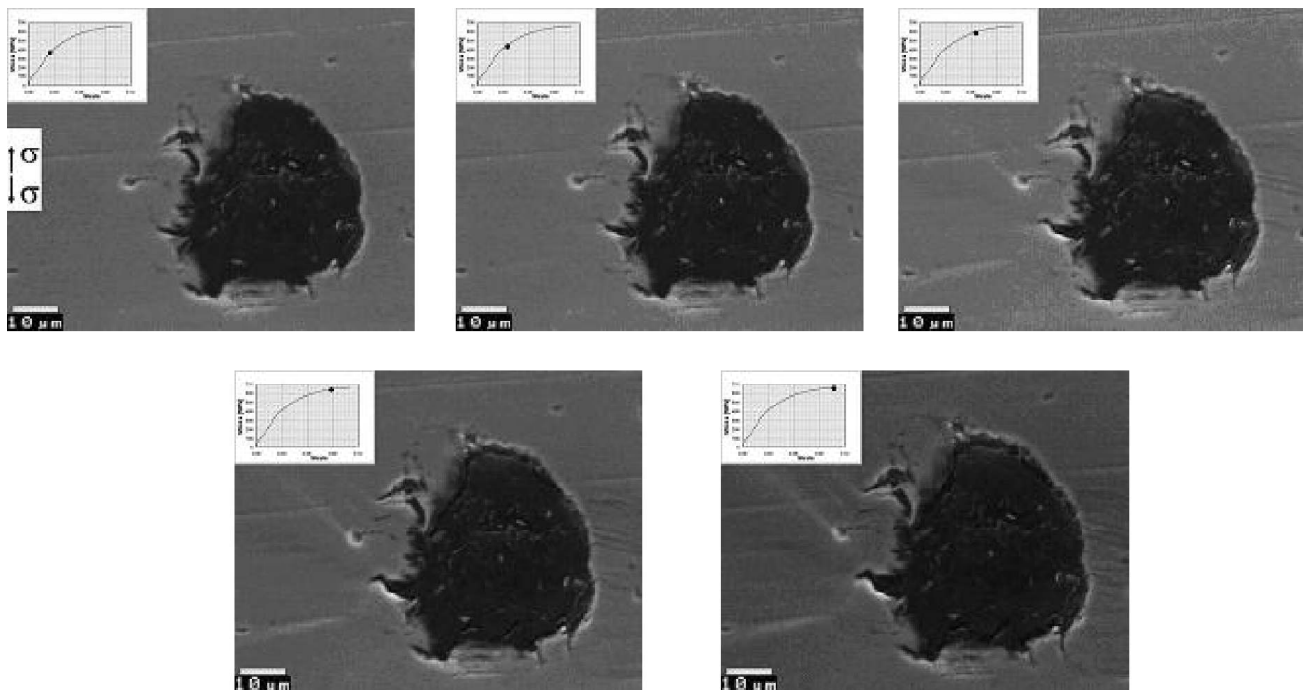


Figure 2: SEM in-situ surface analysis during a tensile test (strain-stress diagram; 50% pearlite-50% ferrite ductile iron): graphite element damage evolution

to the consequent matrix-graphite debonding. Furthermore, a plastic deformation around graphite element becomes more and more evident with the increase of the macroscopic strain. This is due to the peculiar phases distribution (ferritic shields around graphite nodules embedded in a

pearlitic matrix) and to the different mechanical behaviour of ferrite and pearlite. Therefore the material mechanical behaviour can be adequately described once the characterization of both the graphite elements and the microstructure are considered.

3. THE IMAGE SEGMENTATION PROCEDURE

Real data consist in the samples $\{I_{i,j}\}$ of the original image I over a grid of points D . Standard instrumentation provides a 8-bit data measurement, therefore 256 gray levels are available within the conventional range of $[0 \ 1]$. In the considered application an image representation that preserves the relevant information content but with a much lower number of gray levels is advisable. The shape of the image sub-regions with homogeneous gray level gives the information of interest since defines different objects over a common background. Such a simpler representation can be obtained by a piecewise constant image segmentation I_s defined as follows

$$I_s = \sum_{k=1}^K c_k \chi_{D_k}, \quad \chi_{D_k}(i, j) = \begin{cases} 1 & (i, j) \in D_k \\ 0 & \text{otherwise} \end{cases}, \quad B = \left(\bigcup_{k=1}^K \partial D_k \right) \quad (1)$$

where $\{D_k\}$, $k = 1, 2, \dots, K$ is a finite disjoint partition of the image domain D with boundary ∂D , and the c_k 's are the constant values assigned to each sub region D_k ; of course $\partial D \subset B$ where B is the segmentation boundary.

The morphology of the ductile cast iron metallographic planes can be adequately represented by a segmentation with two gray levels (binarization). Let us then consider the case that $D = D_1 \cup D_2$; the two disjoint (not necessarily connected) components D_1 and D_2 can be defined by means of a *level set function*. This is a real valued function $\phi = \{\phi_{i,j}\}: D \rightarrow \mathbb{R}$ defined on the image domain D . By means of the level set function we can define the two image subregions, $D_1 = \{(i, j) : \phi_{i,j} \geq 0\}$, $D_2 = \{(i, j) : \phi_{i,j} < 0\}$. The boundary points of D_1 or D_2 define the boundary B of the segmentation.

It is clear that in the pixels adjacent to any point of ∂D_1 or ∂D_2 the function ϕ has at least one sign change, whereas in the interior points it has none. Let $H(\cdot)$ and $\delta(\cdot)$ denote the Heaviside and the Dirac function respectively. The following function

$$\rho(\phi_{i,j}) = \sum_{\ell=-1}^1 \left[\left(H(\phi_{i+\ell,j}) - H(\phi_{i,j}) \right)^2 + \left(H(\phi_{i,j+\ell}) - H(\phi_{i,j}) \right)^2 \right]$$

counts the number of changes of sign of ϕ in the following neighborhood of pixel $(i, j) : \{(i+1, j), (i-1, j), (i, j+1), (i, j-1)\}$; therefore we can check a boundary point with the following detector:

$$\gamma(\phi_{i,j}) = H(3 - \rho(\phi_{i,j})) \left[1 - \delta(\rho(\phi_{i,j})) \right]$$

Function γ is zero both on interior points ($\rho = 0$) and on isolated points ($\rho = 4$), and is one on the boundary points ($\rho = 1, 2, 3$). Now, given any real data I , segmentation (1) can be obtained by minimizing the following functional

$$E(c_1, c_2; \phi) = \lambda \sum_{i,j} H(\phi_{i,j}) (I_{i,j} - c_1)^2 + \lambda \sum_{i,j} (1 - H(\phi_{i,j})) (I_{i,j} - c_2)^2 + \mu \sum_{i,j} H(\phi_{i,j}) + \nu \sum_{i,j} \gamma(\phi_{i,j}) + \frac{\alpha}{2} \sum_{i,j} \phi_{i,j}^2 \quad (2)$$

This is a discrete version of the early Mumford and Shah variational formulation of the segmentation problem [12]; the first two terms are just the fit error within D_1 and D_2 ; the third and fourth terms evaluate the "area" of D_1 and D_2 and the "length" of the segmentation boundary respectively. Parameters λ , μ and ν are weights that can be used to enhance the contribution of one term with respect to the others. Parameter α weighs the last term that is peculiar of the proposed formulation and is responsible of the functional convexity so that necessary and sufficient conditions for global minimum are available, see [15]. Function E is not smooth with respect to ϕ because of the presence of the generalized functions $H(\cdot)$ and $\delta(\cdot)$. As suggested in [13] we relax the definition of (2) by considering smooth approximants of the generalized functions

$$H(z) \approx H_\varepsilon(z) = \frac{1}{2} \left(1 + \frac{2}{\pi} \tan^{-1} \left(\frac{z}{\varepsilon} \right) \right),$$

$$\delta(z) \approx \delta_\varepsilon(z) = \frac{1}{\pi} \frac{\varepsilon}{\varepsilon^2 + z^2}$$

We therefore modify the definitions of ρ and γ by using H_ε , δ_ε in place of H , δ , and define the following cost function

$$E_\varepsilon(c_1, c_2; \phi) = \lambda \sum_{i,j} H_\varepsilon(\phi_{i,j}) (I_{i,j} - c_1)^2 + \lambda \sum_{i,j} (1 - H_\varepsilon(\phi_{i,j})) (I_{i,j} - c_2)^2 + \mu \sum_{i,j} H_\varepsilon(\phi_{i,j}) + \nu \sum_{i,j} \gamma_\varepsilon(\phi_{i,j}) + \frac{\alpha}{2} \sum_{i,j} \phi_{i,j}^2 \quad (3)$$

Necessary and sufficient conditions for the existence of a unique optimal solution can be found in [15]. The optimal segmentation is given by

$$c_1 = \frac{\sum_{i,j} H_\varepsilon(\phi_{i,j}) I_{i,j}}{\sum_{i,j} H_\varepsilon(\phi_{i,j})}, \quad c_2 = \frac{\sum_{i,j} (1 - H_\varepsilon(\phi_{i,j})) I_{i,j}}{\sum_{i,j} (1 - H_\varepsilon(\phi_{i,j}))} \quad (4)$$

$$0 = \alpha \phi_{i,j} + \left(\lambda p_{i,j} + \mu + \nu \sum_{\ell=-1}^1 \left[(H_\varepsilon(\phi_{i+\ell,j}) - H_\varepsilon(\phi_{i,j})) + (H_\varepsilon(\phi_{i,j+\ell}) - H_\varepsilon(\phi_{i,j})) \right] q_{i,j} \right) \delta_\varepsilon(\phi_{i,j})$$

that is the Euler-Lagrange equation for (3). Functions $p_{i,j}$ and $q_{i,j}$ in (4) have the following definitions

$$p_{i,j} = (I_{i,j} - c_1)^2 - (I_{i,j} - c_2)^2$$

$$q_{i,j} = 2 \left[\begin{aligned} & \delta_\varepsilon(3 - \rho_\varepsilon(\phi_{i,j})) (1 - \delta_\varepsilon(\rho_\varepsilon(\phi_{i,j}))) \\ & - H_\varepsilon(3 - \rho_\varepsilon(\phi_{i,j})) \frac{2\rho_\varepsilon(\phi_{i,j})}{\varepsilon^2 + \rho_\varepsilon^2(\phi_{i,j})} \delta_\varepsilon(\rho_\varepsilon(\phi_{i,j})) \end{aligned} \right]$$

Function ϕ that solves equation (4) is obtained as the limit of a sequence $\{\phi^n\}$ by introducing a fictitious time evolution according to the following finite difference evolution equation

$$\begin{aligned} \phi_{i,j}^{n+1} = & -\frac{1}{\alpha} \left[\lambda p_{i,j}^n + \mu + \nu q_{i,j}^n \left(\left(H_{\varepsilon}(\phi_{i-1,j}^n) - H_{\varepsilon}(\phi_{i,j}^n) \right) + \left(H_{\varepsilon}(\phi_{i+1,j}^n) - H_{\varepsilon}(\phi_{i,j}^n) \right) \right) \right. \\ & \left. + \left(H_{\varepsilon}(\phi_{i,j-1}^n) - H_{\varepsilon}(\phi_{i,j}^n) \right) + \left(H_{\varepsilon}(\phi_{i,j+1}^n) - H_{\varepsilon}(\phi_{i,j}^n) \right) \right] \delta_{\varepsilon}(\phi_{i,j}^n) \end{aligned} \quad (5)$$

where $p_{i,j}^n$ and $q_{i,j}^n$ are functions $p_{i,j}$ and $q_{i,j}$ computed by replacing in their expression $\phi_{i,j}$ by $\phi_{i,j}^n$. The solution of (5) converges to the solution of (4) whatever the initial condition [15].

Equation (5) provides an explicit scheme for the computation of the exact level set function $\{\phi_{i,j}\}$: the value in the pixel (i, j) at step $n + 1$ is function of the values in neighbouring pixels at step n ; therefore only one level of recursion is required as the “time” n increases to achieve the steady-state. Convergence is quite fast and makes the algorithm eligible for real time applications.

The level set function approach is a region based algorithm able to deal with the complex topology of the real world images as the level set function evolves according to equation (5) from an arbitrary initial configuration toward the steady-state function that yields the optimal segmentation, see Fig. 3.

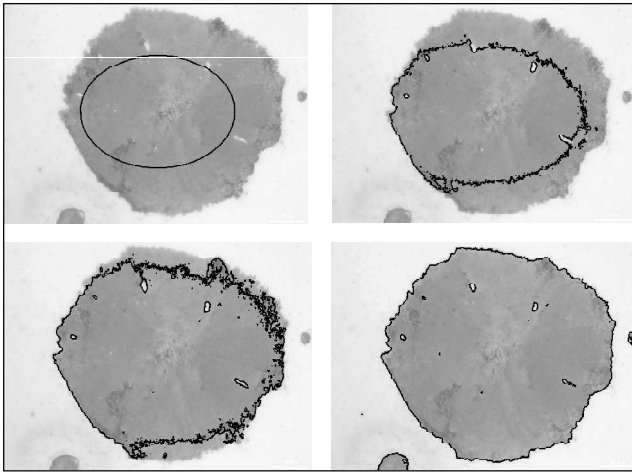


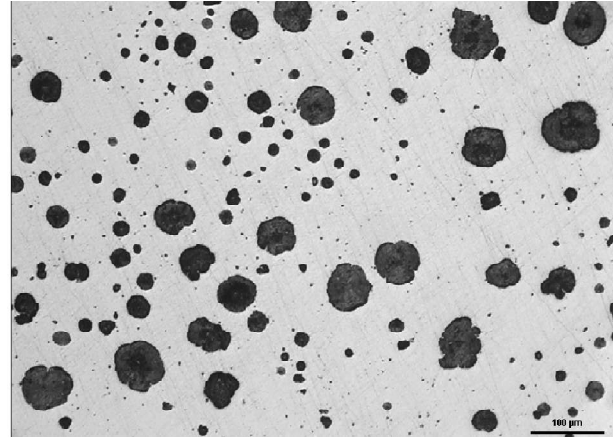
Figure 3: Zero level set evolution from an arbitrary initial configuration to the final configuration giving the optimal segmentation at step 20

A rationale for the choice of the weight parameters can be found in [15], where it is shown that the algorithm performance is by far more affected by parameter λ ; as a general guideline the finer the contrast the larger λ .

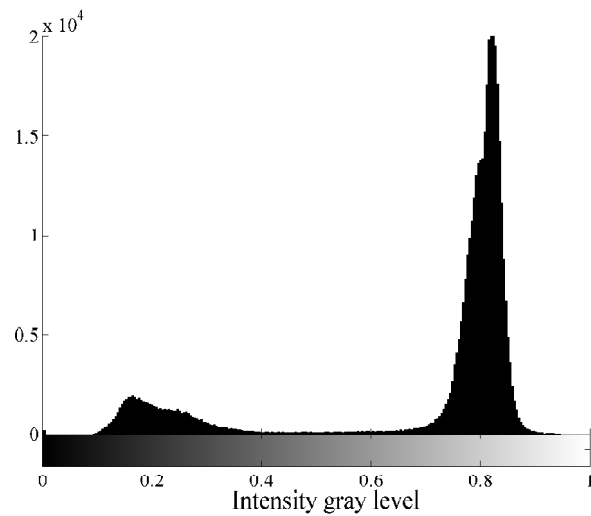
4. DUCTILE CAST IRON DATA ANALYSIS

A key point in the characterization of the ductile cast irons is the morphological analysis of the graphite nodules. Therefore the first task consists in separating the spheroids from the background; this can be obtained by binarizing the material specimens pictures. It is known that the simplest image binarization procedure is based on a thresholding processing, the threshold being designed by histogram

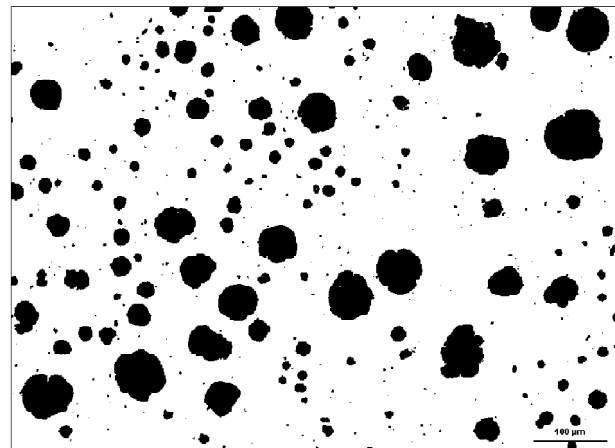
analysis. Such a method may be very effective providing that the intensity histogram has a typical bimodal shape, as in the case of the specimen on Fig.4a; here the threshold can be computed as the mean value of the modes abscissas. Fig.4c shows a satisfactory binarization. On the contrary,



(a)



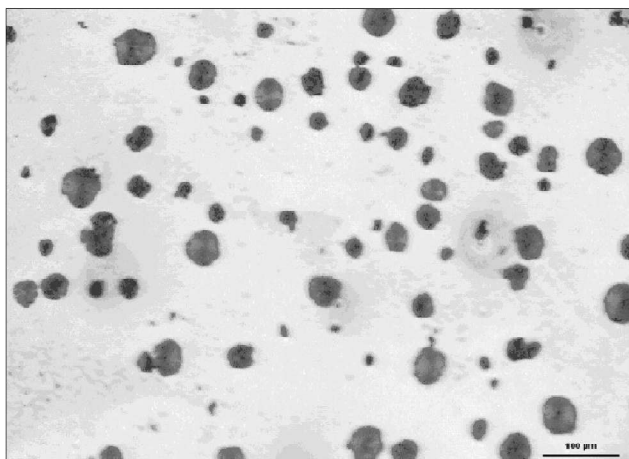
(b)



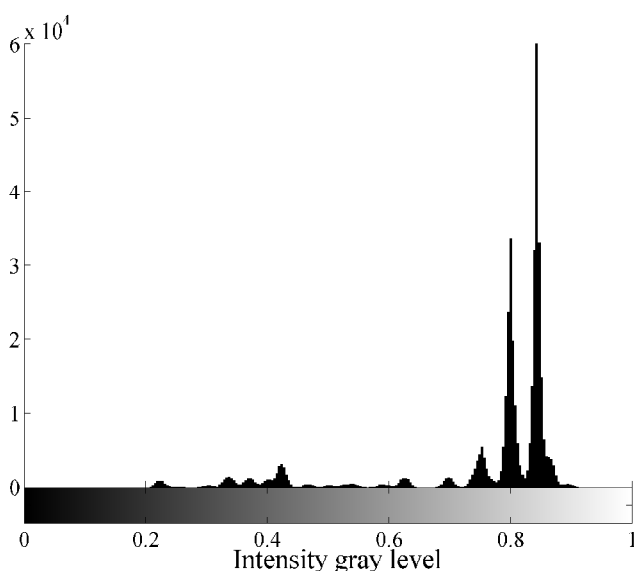
(c)

Figure 4: Binarization by histogram analysis. (a) Original image; (b) Intensity histogram; (c) Binarization with a threshold equal to 0.5

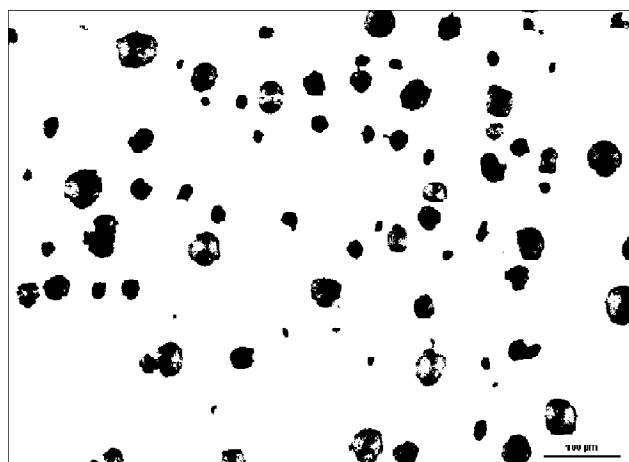
the histogram of Fig.5a denotes a very irregular gray level distribution, and the automatic determination of a suitable threshold is questionable. Of course it can be chosen manually within few attempts.



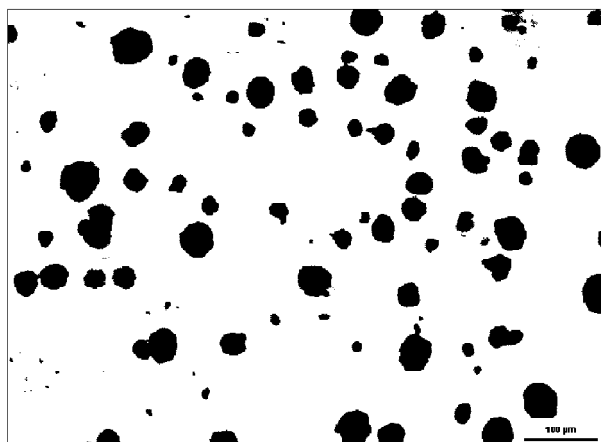
(a)



(b)



(c)



(d)

Figure 5: Binarization by histogram analysis. (a) Original image; (b) Intensity histogram; (c) Binarization with a threshold equal to 0.45; (d) Binarization with a threshold equal to 0.65

Specimens of a large production have an unpredictable gray level distribution, therefore a reliable segmentation procedure is required for morphological analysis, such as the region based algorithm proposed.

The morphological characterization of ductile cast irons is based on parameters such as: the nodules size, solidity and eccentricity that characterize the nodule roundness, the degree of granularity, that describes how the nodules are distributed over the metallic matrix area. In a material of good quality the nodules are uniformly distributed over the matrix, and have a high solidity along with low eccentricity values, Fig. 6a. As opposite Fig. 6c represents a deformed nodule with very low solidity and surely not round. In Fig. 6b an intermediate situation is shown where, due to the nodule contour roughness, solidity decreases with respect to Fig 6a, whereas we still have a good degree of roundness.

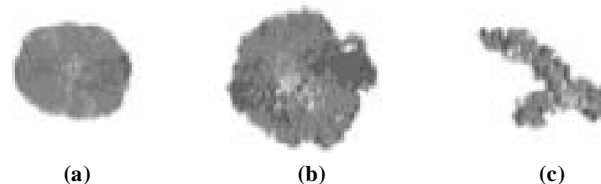
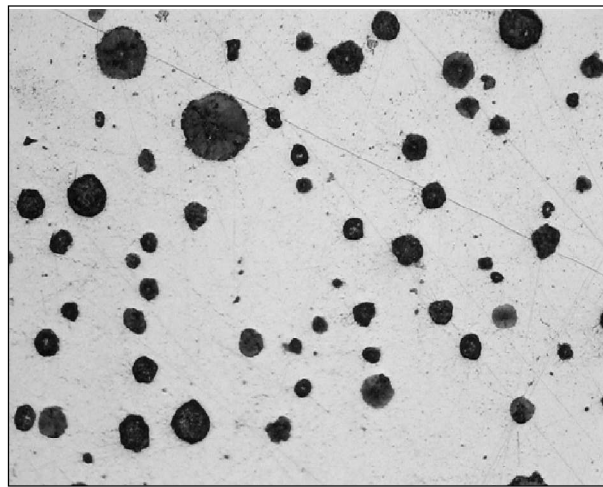


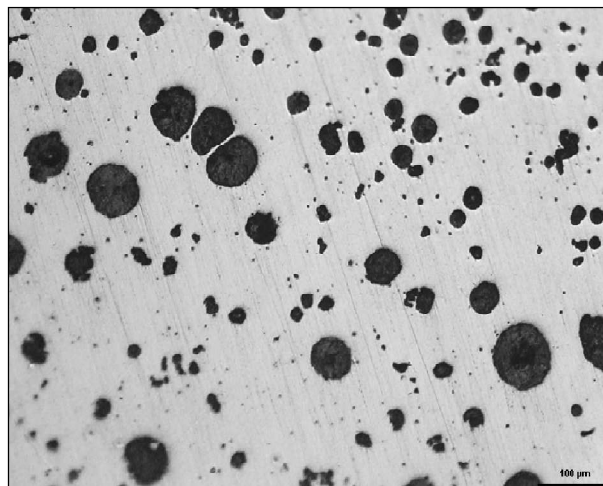
Figure 6: Some typical graphite nodules

In Fig. 7 three specimens with different degrees of granularity, with nodules area values and spatial distribution varying in a large range of situations are displayed: in the specimen of Fig. 7a the nodules are better distributed as compared to those on Fig. 7c. The specimen on Fig. 7b has an intermediate degree of granularity as compared to the others.

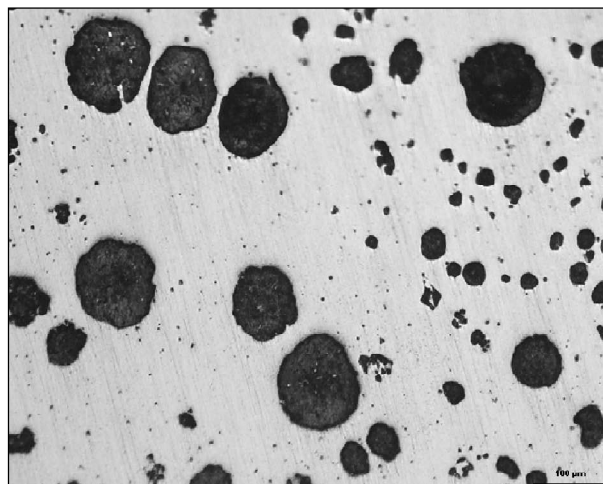
Our discussion about the specimens of Figs.6 and 7 is just what an expert does by visual inspection. It is therefore of paramount importance to give a standard quantitative evaluation of the nodules shape characteristics, especially in real situations where, on the same specimen, nodules with characteristics shifting between the cases shown in Fig.6 are present. To this aim a specimen binarization can be



(a)



(b)



(c)

Figure 7: Specimens with different degrees of granularity.
(a) good; (b) medium; (c) low

performed to separate the nodules from the background. For binarized images, the Matlab Image Processing Toolbox provides functions to label all the objects over the background; therefore, once the pixel list of any nodule is

available, the morphological properties of interest can be evaluated. The nodule size is described by the Area parameter that is defined simply by its number of pixels. The Solidity parameter is computed as the ratio between the nodule Area and the area of its convex hull; therefore Solidity values range in $[0, 1]$. The Eccentricity parameter is defined as the eccentricity of the ellipse that best fits the nodule, and its values also range in $[0, 1]$. For example, the nodule of Fig. 6a has Solidity close to 1 and Eccentricity close to 0, as opposite to the nodule of Fig.6c whose Solidity is below 0.3 and the Eccentricity is about 0.8; the nodule of Fig.6b has a good Eccentricity but Solidity lower than the nodule of Fig. 6a.

The accurate estimation of these shape parameters is strongly affected by the binarization quality. The performance of the proposed procedure (discrete level set approach, DLS) has been assessed versus the performance of the well established region based segmentation procedure in [13] (continuous level set approach, CLS), whose outcome was used as ground truth data. In both procedures, the typical algorithm parameters have been chosen at their own best. The test is based on an *object-to-object* comparison by evaluating the differences in the estimates of the shape parameters of interest, and on the ratio of the DLS over the CLS speed. A batch of 88 specimens (each one containing on average 50 nodules of significant size) was considered; the results are summarized in Table 1. In the first column median μ and standard deviation σ of the area error normalized to the area measured by the CLS method are reported; in the second and third column the medians and standard deviations of the errors of Solidity and Eccentricity are displayed.

Table 1
Statistics of the Comparison between the CLS and DLS Performances

Area error	Solidity error	Eccentricity error	Speed ratio
$\mu = -0.067$	$\mu = -0.0431$	$\mu = -0.0072$	$\mu = 2.0342$
$\sigma = 0.0087$	$\sigma = 0.0029$	$\sigma = 0.0051$	$\sigma = 0.0169$

From data on the fourth column of Table 1 it can be noted that the DLS procedure is as double as faster than the CLS one, already in a binarization process; moreover the errors are negligible, meaning that the parameters DLS estimates are as much as accurate of those of the benchmark CLS method.

We finally proceeded in applying the DLS procedure to the required morphological study of ductile cast irons. A first level of analysis was aimed to the characterization of the graphite nodules shape and distribution. The procedure parameters were set to this values: $\varepsilon = 1$, $\lambda = 10^3$, $\mu = 1$, $\nu = 1$, and $\alpha = 1$

Fig. 8 displays the binarization of the specimen of Fig.7a. For any nodule the shape parameters were evaluated; for simplicity, the set of values just for two nodules are reported in the picture.

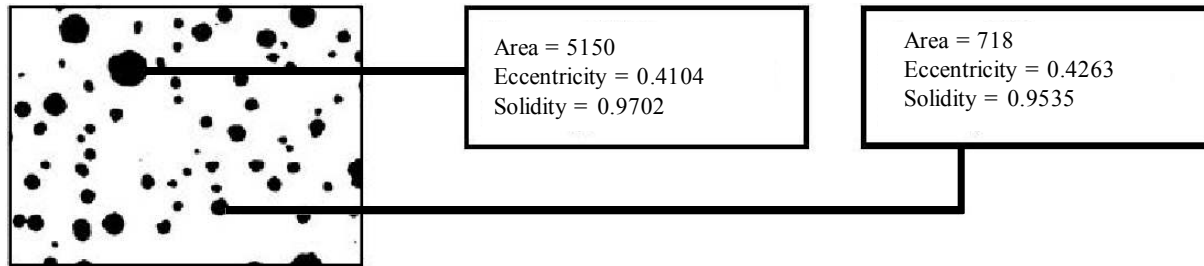


Figure 8: Optimal binarization of specimens of Fig. 7a with shape parameters values for two different nodules

To provide an overall evaluation of the quality of the material specimens of Fig. 7 we determine the sample distribution of the nodules over the values of Area, Solidity and Eccentricity; in Fig. 9 the histograms for the specimen of Fig. 7a are reported.

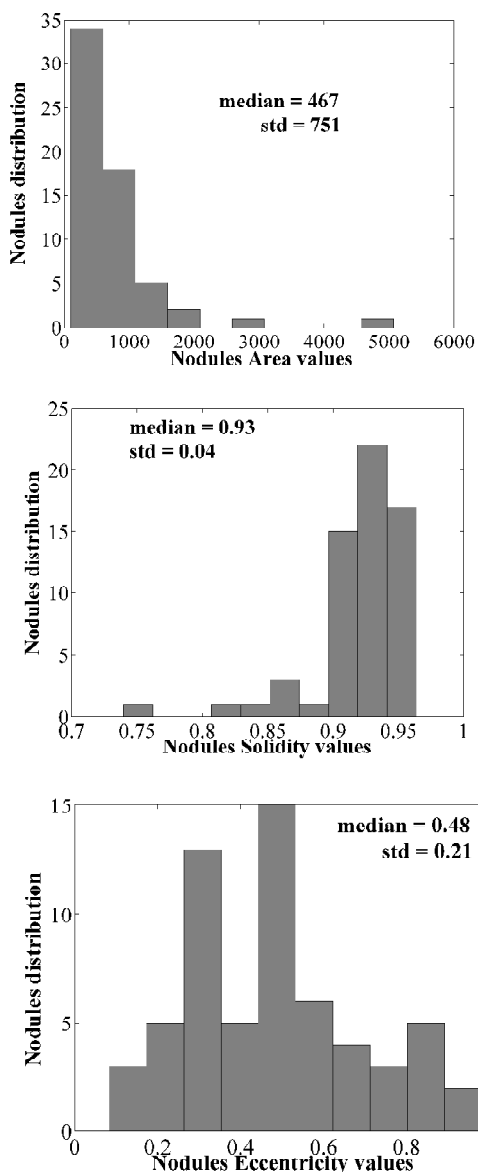


Figure 9: Sample distribution of Area, Solidity and Eccentricity of specimen of Fig. 7a.

Standard averages can be computed for Area, Solidity and Eccentricity for the specimens of Fig. 7 and are reported in Table 2. Hence the operator can obtain a specimen signature to classify the quality of the current ductile cast iron production. To characterize Granularity we introduced the following indicators:

- N : the number of nodules in the specimen;
- ND : the number of nodules per unit area;
- CV_AREA : the coefficient of variation (i.e. standard deviation over the mean) of the nodules area distribution;
- CV_ND : the coefficient of variation of the nodules local density. The specimen area is tiled into 9 equal subregions; in each tile the local nodules density is computed and the error with respect to the global density ND is evaluated. The standard deviation of this quantity over ND defines CV_ND .

In Table 2 the median μ and the standard deviation σ of Area, Solidity, Eccentricity are reported along with the Granularity indicators of specimens of Fig. 7.

The values in Table 2 were obtained by disregarding nodules with area lower than 100 pixels; these indeed correspond either to dust inclusion during the specimen preparation or to nodules at different metallographic planes. Data in Table 2 show that the specimens of Fig. 7a has a better Granularity than that of Fig. 7c, as all the indicators are better: higher ND , lower CV_AREA (meaning a larger number of similar nodules, that is with Area values closer to the average Area value), lower CV_ND (that is the nodules local density is more similar to the nodules global density, denoting a better distribution over the specimen surface). The specimen of Fig. 7b has an intermediate ranking: despite a higher global nodules density (due to a higher number of nodules), their spatial distribution is worse as compared to that of specimen of Fig. 7a (higher CV_ND), moreover there is a larger dissimilarity in the nodules size, as the CV_AREA parameter is greater. As a further test we analyze the specimen of Fig. 10 that, by visual inspection, shows a good Granularity but with not well-formed nodules.

Table 2
Morphological and Granularity Parameters of Specimens of Fig. 7

	<i>Area</i>	<i>Solidity</i>	<i>Eccentricity</i>	<i>N</i>	<i>ND</i>	<i>CV_AREA</i>	<i>CV_ND</i>
Specimen of Fig.7a	$\mu = 467$ $\sigma = 751$	$\mu = 0.93$ $\sigma = 0.04$	$\mu = 0.48$ $\sigma = 0.21$	61	1.48	1.08	0.34
Specimen of Fig.7b	$\mu = 283$ $\sigma = 759$	$\mu = 0.92$ $\sigma = 0.07$	$\mu = 0.62$ $\sigma = 0.19$	89	2.16	1.3	0.37
Specimen of Fig.7c	$\mu = 404$ $\sigma = 2420$	$\mu = 0.92$ $\sigma = 0.09$	$\mu = 0.60$ $\sigma = 0.18$	52	1.26	1.62	0.68

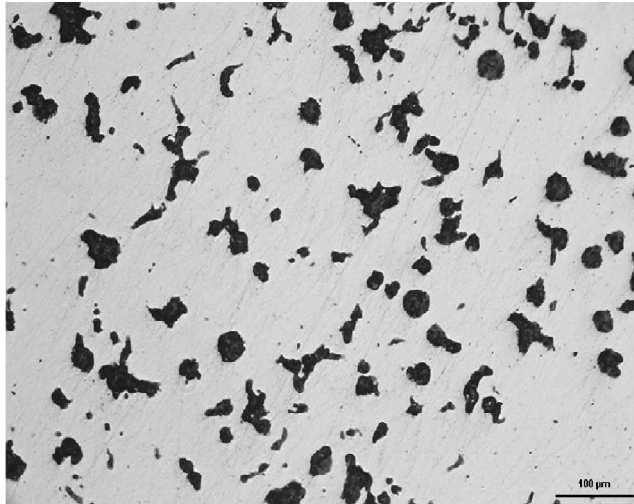


Figure 10: Specimen with good granularity but not well formed nodules

Table 3
Morphological and Granularity Parameters of Specimens of Fig. 10

<i>Area</i>	<i>Solidity</i>	<i>Eccentricity</i>	<i>N</i>	<i>ND</i>	<i>CV_AREA</i>	<i>CV_ND</i>
$m = 434$	$m = 0.83$	$m = 0.77$	87	2.11	0.72	0.27
$s = 392$	$s = 0.12$	$s = 0.20$				

In fact, data in Table 3 characterize a specimen with a good nodules distribution: *CV_AREA* is lower than that of the specimens of Fig.7, this denoting that there is a larger number of nodules with similar area; *CV_ND* is again lower as compared to data for Fig.7, meaning that the nodules local density is closer to the nodules global density. Nevertheless the nodules shape has worse indicators with respect to the

nodules of the specimens of Fig.7: Solidity has a lower median value whereas Eccentricity has a higher median value denoting a significant decrease in the nodules roundness.

A second level of analysis consisted in determining the characteristics of the metallic matrix, that depend on the phases volume fractions. Different etching conditions (e.g. solution chemical composition, temperature or etching duration) allow to mark differently each phase. Light areas correspond to ferrite, gray areas correspond to pearlite and black nodules correspond to graphite. In order to evaluate the ferrite/pearlite ratio it is necessary to measure the ratio between the light/gray area to the total available area (light plus gray area). To this aim it is necessary to measure the area of the ferritic phase: this can be obtained from the specimen binarization by subtracting from the specimen area the total area of the black objects; these ones are either nodules or the dark gray areas relative to the pearlite phase. To evaluate the ferrite volume fraction we further need to determine the total area of the matrix, that is the specimen area out of the nodules. To this aim we need to select among the black elements of the specimen binarization those that correspond to the nodules: this can be done by using the shape parameters estimated as in the previous analysis; the nodules indeed can be extracted by the degree of roundness defined by the Solidity and the Eccentricity. In the following the results obtained for four typical cast iron specimens are reported: for any specimen the original picture, the optimal binarization and the selected nodules are displayed.

In Figs. 11-14 the nodules were selected according to the following procedure: the median and standard deviation of the Eccentricity values were computed; hence the nodules were identified as those elements in the binarized image with Solidity not less than 0.9 and Eccentricity below $m_E + 0.5$

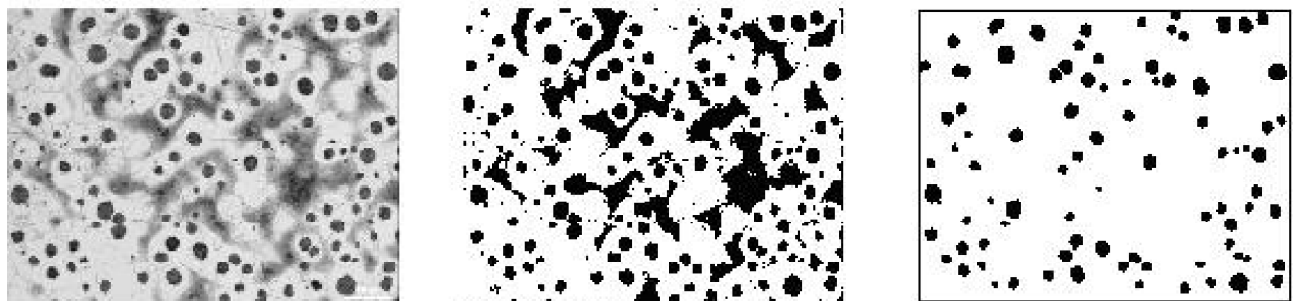


Figure 11: (a) original image with 70% of ferrite (expert's evaluation); (b) binarization; (c) selected nodules

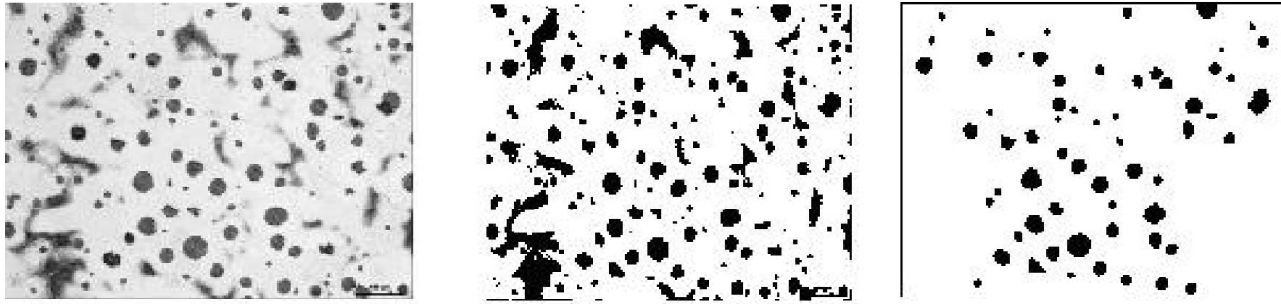


Figure 12: (a) original image with 80% of ferrite (expert's evaluation); (b) binarization; (c) selected nodules

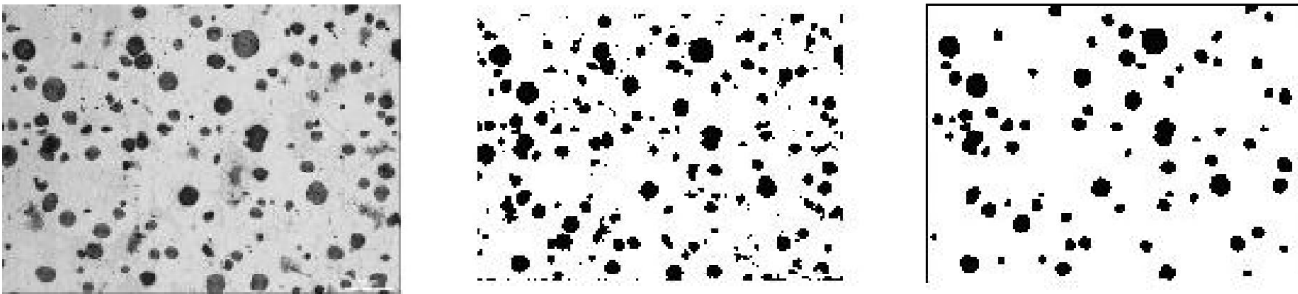


Figure 13: (a) original image with 90% of ferrite (expert's evaluation); (b) binarization; (c) selected nodules

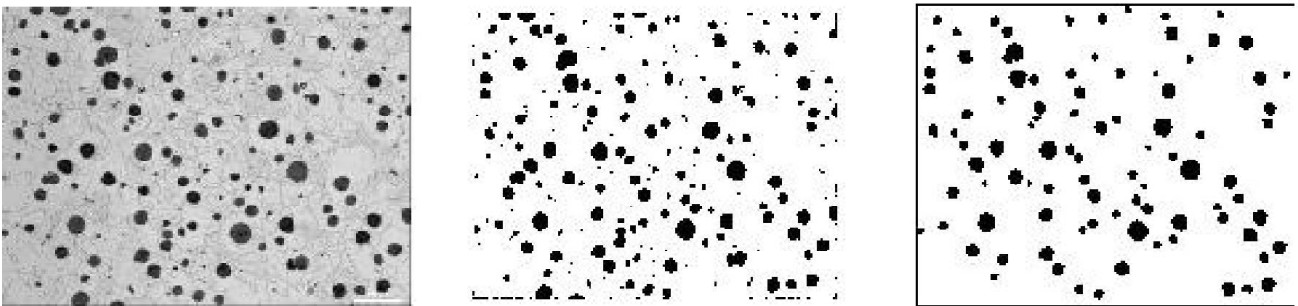


Figure 14: (a) original image with 100% of ferrite (expert's evaluation); (b) binarization; (c) selected nodules

σ_E . The thresholds were chosen by trial error procedure on a large batch of metallographic specimens, according to the experts suggestions, in order to obtain a reliable phase volume fraction evaluation. The ferrite phase volume fraction was then evaluated as 79%, 88%, 92% and 100% respectively as compared to the expert's visual classification of 70%, 80%, 90% and 100%. The estimates obtained by the proposed procedure are reliable since, as can be observed, both the light areas corresponding to the ferrite phase and the nodules that allow to quantify the total matrix surface available to etching are reliably evaluated from the binarized image.

5. CONCLUSIONS

In this work a novel discrete set up to the image segmentation problem was proposed and applied to the analysis of the geometry of the ductile cast iron metallographic specimens. A robust estimation procedure was devised for a quantitative evaluation of parameters describing the morphology of the

material microstructure and nodules shape. These estimates provide a rich set of standard geometrical characteristics that may support the experts in the quality evaluation of ductile cast iron productions. As a further development, any supervised learning technique can be enforced by using the geometrical properties of the cast iron nodules and microstructure to evaluate the material quality directly in terms of its mechanical characteristics.

REFERENCES

- [1] Suri, J. S., Liu, K., Singh, S., Laxminarayan, S. N., Zeng, X. and Reden, L. (2002), Shape Recovery Algorithms Using Level Sets in 2-D/3-D Medical Imagery: A State -of-the-Art Review. *IEEE Trans. on Inform. Tech. in Biomedicine*, 6(1): 8-28.
- [2] Sund T., Eilertsen K. (2003), An algorithm for fast adaptive image binarization with applications in radiotherapy imaging. *IEEE Trans. Med. Imaging* 22: 1-8.
- [3] Dellepiane, S.; Bo, G.; Monni, S.; Buck, C. (2000), SAR images and interferometric coherence for flood monitoring. *IEEE Proc. of the Int. Geoscience and Remote Sensing Symposium*, 24-28 July 2000, 6: 2608-2610.

- [4] Hutchinson, T. C.; Kuester, F. (2004), Monitoring global earthquake-induced demands using vision-based sensors, *IEEE Trans. on Instrumentation and Measurements*, 53 (1): 31-36.
- [5] Pang, C.C.C., LAM, W. W. L., and Yung, N. H. C. (2004), A novel method for resolving vehicle occlusion in a monocular traffic-image sequence, *IEEE Trans. on Intelligent Transportation Systems*, 5 (3) : 129-141.
- [6] Landabaso, J. L., LI-Qun XU, and Pardas, M. (2004), *Robust Tracking and Object Classification Towards Automated Video Surveillance*, Lecture Notes in Computer Science, Springer-Verlag.
- [7] Kumar, A. and G. Pang (2002), Defect detection in textured materials using gabor filters. *IEEE Transactions on Industry Applications*, 38 (2).
- [8] Latif-Amet, A., A. Ertuzun, and A. Ercil (2000), An efficient method for texture defect detection: Sub-band domain co-occurrence matrices. *Image and Vision Computing* 18 (6): 543–553.
- [9] Imasogie, B. I., Wendt, U. (2004), Characterization of Graphite Particle Shape in Spheroidal Graphite Iron Using a Computer Based Image Image Analyzer. *Journal of Minerals and Materials Characterization & Engineering*, 3 (1): 1-12.
- [10] Jianming Li, Li Lu, Man On Lai. (2000), *Materials Characterisation*. 45: 83-88.
- [11] A. De Santis, O. Di Bartolomeo, D. Iacoviello, F. Iacoviello, 2007, Optimal Binarization of Images by Neural Networks for Morphological Analysis of Ductile Cast Iron, *Pattern Analysis and Applications*, 10(2): 125-133.
- [12] Mumford, D., Shah, J. (1989), Optimal approximations by piecewise smooth functions and associated variational problems. *Comm. Pure Appl. Math.* 42 (4).
- [13] Chan, T., Vese, L. (2001), Active Contours Without Edges. *IEEE Trans. on Image Processing*, 10 (2): 265-277.
- [14] Morel, J. M., Solimini, S. (1995), *Variational Methods in Image Segmentation (Part I)*, *Progress in Nonlinear Differential Equations and Their Applications*, 14 Boston MA., Birkhauser .
- [15] De Santis, A., Iacoviello, D. (2007), Discrete level set approach to image segmentation. *Signal, Image and Video Processing*, 1(4): 303-320.
- [16] Iacoviello, F., Di Cocco, V. (2003), Fatigue crack paths in ferritic-pearlitic ductile cast irons, *Proceedings of International Conference on Fatigue Crack Paths*, Parma, Italy, 116: 18-20.